Nuclear Instruments and Methods in Physics Research B30 (1988) 191–195
North-Holland, Amsterdam

THE SECONDARY-ELECTRON YIELD MEASURED FOR 5–24 MeV PROTONS ON ALUMINUM-OXIDE AND GOLD TARGETS

Joseph E. BOROVSKY, David J. McCOMAS, and Bruce L. BARRACLOUGH

Space Plasma Physics Group, Los Alamos National Laboratory, Los Alamos, NM 87545, USA

Received 26 August 1987

The yield of first-surface secondary electrons from H^+ impact on aluminum and gold targets is measured. Data are obtained for proton energies of $5 \leq E \leq 24$ MeV on aluminum and $5 \leq E \leq 18$ MeV on gold, and these data are compared with theoretical expectations and with previous data for lower proton energies. An empirical curve for the yield from aluminum-oxide is obtained from a theoretical curve for pure aluminum by using earlier measurements of primary-electron-produced yields from both aluminum and aluminum-oxide.

1. Introduction

Secondary-electron emission is the dominant surface yield when MeV-energy protons enter metallic targets, with the yields of sputtered ions or reflected protons being insignificant. The source of these electrons is the Coulomb interaction of the fast protons with electrons within about 100 Å of the surface of the target [1]. Only a very small number of experiments have measured the secondary-electron yield for MeV-energy primary ions [2], and these have been limited to ion energies less than 7.5 MeV. In the experiment described here, the secondary-electron emission coefficient is measured for 5–24 MeV protons from the Los Alamos National Laboratory three-stage Van de Graaff accelerator passing through aluminum-oxide and gold surfaces.

2. Apparatus

A sketch of the experimental apparatus appears in fig. 1. Here a proton beam with a known flux and energy is normally incident on a flat target is biased to a negative potential (−300 V) with respect to ground. The target is thick enough to stop the protons of the beam, so the total current from ground to the target required to maintain its potential is equal to the beam current plus the current of secondaries. The yield of secondary electrons (number of secondary electrons produced per proton impact) is thus

$$Y = \frac{I_{\text{total}} - I_{\text{beam}}}{I_{\text{beam}}}. \qquad (1)$$

The targets reside in a cylindrical co-netic-metal chamber that has a radius of ~19 cm. The magnetic-field strength inside the chamber is measured to be $B \sim 0.2$ G. With an average electric-field strength of $E \approx 300$ V/19 cm $= 4.5 \times 10^{-3}$ statvolt/cm between the biased target and the chamber wall, a zero-energy electron leaving the target surface is repelled to a distance $d = 2(cE/B)/(eB/m_e c) = 9.2 \times 10^2$ cm away from the target before the magnetic field brings it back (the Hull cutoff distance [3].) Since $d \gg 19$ cm, no secondary electrons are magnetically returned to the target. (A bias of −20 V was found to force about half of the secondaries from the targets and a bias of −80 V was found to force essentially all of the secondaries away.)

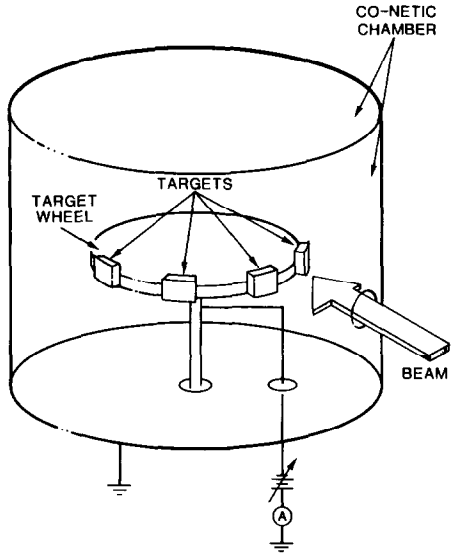

Fig. 1. A sketch of the targets in the co-netic metal chamber.

The sputtered-ion contribution to the current is

negligible in the 5–19 MeV range of proton energies. For H^+ kinetic energies of 8 keV, the experimentally measured sputtering yield for aluminum targets is about 3×10^{-3}, and this yield decreases rapidly with H^+ energy (see fig. 4.7 of Andersen and Bay [4]). For H^+ kinetic energies of 20 keV on gold targets, the experimentally measured sputtering yield is about 8×10^{-3}, and this yield also decreases rapidly with H^+ energy [5]. The fraction of incident protons that are reflected from the surface of the targets is miniscule, as indicated in fig. 3 of ref. [6], so this associated current is also negligible. The ranges of $E \leq 24$ MeV protons are ≤ 3.3 mm in Al and the ranges of $E \leq 18$ Mev protons in Au are ≤ 0.47 mm [7]. Since these ranges are considerably less than the target thicknesses (Al = 6.44 mm and Au = 0.79 mm), essentially no protons reach the back of the targets and, hence, second-surface effects (transmission sputtering and secondary-electron emission) do not contribute to the target currents.

The aluminum target is a piece of extruded 6061 alloy (1.0% Mg, 0.6% Si, 0.25% Cu, and 0.25% Cr) that was not heat-treated. Because it was extruded hot, it is anticipated that the aluminum target has a surface layer of Al_2O_3 which is 50–1000 Å thick [8–10], and because the 6061 alloy has 1.0% Mg, it is possible that this surface contains a significant amount of magnesium-oxide [11]. The gold target is a piece of cold-rolled sheet that is 99.9% pure. It is believed that the gold target does not have an oxide surface. The targets were degreased with 1,1,1 trichloroethane before being placed in the target chamber, whose base pressure is $1–2 \times 10^{-5}$ Torr. Typical beam currents are 10^{-8} A, which are insufficient to clean any surface coatings from the targets. Since the momentum-exchange cross section for low-energy electrons in N_2 gas [12] is $< 3.5 \times 10^{-15}$ cm^2/molecule, the mean free path L for an electron in 2×10^{-5} Torr of air (1 Torr ~ 3×10^{15} molecules/cm^3) is $L = 1/n\sigma > 4.7 \times 10^3$ cm^3 cm. Hence, the chamber air does not hinder the passage of secondary electrons from the target to the chamber walls (which are ~ 19 cm away).

The beam current on target is determined by moving the target out of the beam and measuring the beam current via a high-aspect ratio Faraday cup. Temporal fluctuations in the beam current put out by the Van de Graaff during this procedure account for the major portion of the scatter in the yield data.

3. Measured secondary-electron yields

The measured secondary-electron yields for H^+ on oxidized aluminum and for H^+ on gold are contained in table 1. These yields are plotted (solid points) as functions of the proton kinetic energy in figs. 2 and 3 for

Table 1
The measured secondary-electron yields for protons striking the front surface of aluminum and gold targets

Proton energy (MeV) (MeV)	Yield
Oxidized aluminum	
5	0.64
7	0.50
9	0.49
11	0.39
13	0.35
15	0.29
17	0.27
17.5	0.23
18	0.25
19	0.20
24	0.15
Gold	
5	0.58
7	0.48
9	0.47
11	0.36
13	0.31
15	0.27
17	0.33
17.5	0.22
18	0.26

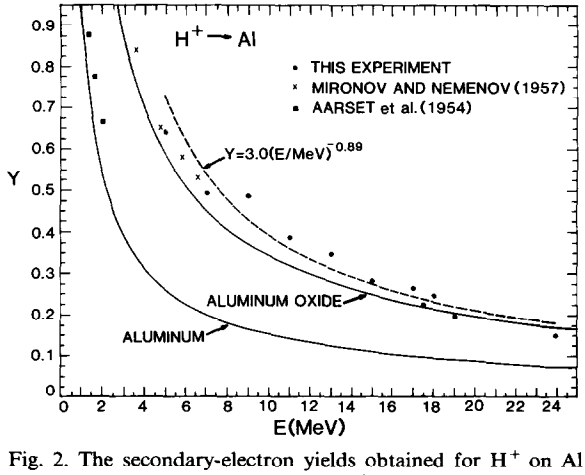

Fig. 2. The secondary-electron yields obtained for H^+ on Al are plotted versus the energy of the H^+ (solid points) and a fit to this data is drawn as the dashed curve. Also plotted are some earlier measurements of the yields (refs. [13] and [14]). The solid curves (eqs. (4) and (6) are theoretical estimates for the yields (see text).

aluminum and gold, respectively. Least-square fits to the log(Y) versus log(E) data yield

$$Y_{Al_2O_3} = 3.0\left(\frac{E}{\text{MeV}}\right)^{-0.89} \qquad 5 \le E \le 24 \text{ MeV} \qquad (2)$$

for aluminum-oxide and

$$Y_{Au} = 1.8\left(\frac{E}{\text{MeV}}\right)^{-0.67} \qquad 5 \le E \le 18 \text{ MeV} \qquad (3)$$

for gold, which are plotted as the dashed lines in the two figures. The rms scatter of the yield data about these fits are $\pm 9.3\%$ for aluminum and $\pm 10.7\%$ for gold. Also included in the figures are the $H^+ \rightarrow$ Al data of Mironov and Nemenov [13] and some $H^+ \rightarrow$ Al and $H^+ \rightarrow$ Au data of Aarset et al. [14]

Theoretical predictions of the secondary-electron yield for fast ions normally incident on aluminum and gold surfaces are plotted as a solid curves in figs. 2 and 3. These curves are obtained from eq. (17) of Sternglass [15]. For aluminum (fig. 2) the quantities used (see ref. [15]) in that equation are $\tau A = 0.5$, $\alpha' = 0.23$, $\sigma_g = 4.4 \times 10^{-16}$ cm^2, $E_0 = 25$ eV, and $N = 6.0 \times 10^{22}$ cm^{-3}, which results in

$$Y_{Al} = 1.6 \times 10^{-9}\left(\frac{dE/dx}{\text{eV/cm}}\right)\left[1 + \frac{1}{1 + \frac{E}{0.183 \text{ MeV}}}\right]. \qquad (4)$$

For gold the quantities used in eq. (17) of Sternglass are $\tau A = 0.5$, $\alpha' = 0.23$, $\sigma_g = 7.0 \times 10^{-16}$ cm^2, $E_0 = 25$ eV, and $N = 5.9 \times 10^{22}$ cm^{-3}, which results in

$$Y_{Au} = 1.1 \times 10^{-9}\left(\frac{dE/dx}{\text{ev/cm}}\right)\left[1 + \frac{1}{1 + \frac{E}{0.183 \text{ MeV}}}\right] \qquad (5)$$

as the predicted secondary-electron yield. For the theoretical curves in figs. 2 and 3, eqs. (4) and (5) are used with the electronic stopping powers dE/dx for H^+ in aluminum and gold as given by Northcliffe and Schilling [16] for energies of 12 MeV and lower and with the stopping powers as given by Littmark and Ziegler [7] for 12 MeV and higher. Note that the mean free path of a secondary electron is $L_s = 1/\alpha' N \sigma_g = 16.4$ Å within aluminum and is $L_s = 10.5$ Å within gold. These mean free paths are approximately the thickness of the surface layers from which the emitted secondary electrons originate. The theoretical secondary-electron-yield curve for aluminum-oxide in fig. 2 will be discussed below.

The $H^+ \rightarrow$ Al data obtained in this experiment agree well with the lower-energy data of Mironov and Nemenov [13] (see fig. 2). This is not surprising, since both experiments were performed under similar vacuum conditions and similar target-cleaning procedures were carried out. It is thought that the aluminum targets used in the Mironov and Nemenov experiment, as well as those of this experiment, had surfaces that were predominantly aluminum-oxide Al_2O_3. The aluminum data of Aarset et al. [14] (see fig. 2) were obtained after proton bombardment of the targets for more than two hours at $\sim 5 \times 10^{-7}$ A of beam current, a procedure which was not followed in the present experiment. Presumably, this persistent bombardment removed any aluminum-oxide from the surface and reduced the amount of other surface contaminants. Clearly, the trend of the data from the Aarset et al. experiment is toward lower yields than is the trend of data of the present experiment, and the Aarset et al. data are in better agreement with the theoretical aluminum curve.

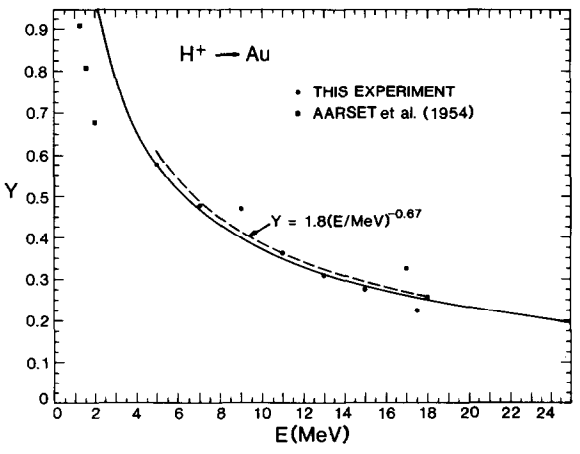

Fig. 3. The secondary-electron yields obtained for H^+ on Au are plotted versus the energy of the H^+ (solid points) and a fit to this data is drawn as the dashed curve. Also plotted are some earlier measurements of the yields (ref. [14]). The solid curve (eq. (5)) is a theoretical estimate for the yields (see text).

According to Sternglass [15], the yield of secondary electrons produced by fast protons in the material is proportional to $(dE/dx)L_s$, where dE/dX is the stopping power of the proton in that material and where L_s is the mean free path of a secondary electron within that material. The dE/dx is a measure of how many secondary electrons are produced within the material and L_s is a measure of the depth from which these secondary electrons are able to escape to the surface of the material. Since [17] $dE/dx \propto nZ$ for proton energies exceeding a few hundred eV (where n is the atomic density of the material and where Z is the atomic number of the material), the stopping power of Al_2O_3 relative to that of Al is $(dE/dx)_{Al_2O_3} \simeq 0.95(dE/dx)_{Al}$. This indicates that the number of electrons knocked lose as protons pass through the two materials is about the same. Consequently, the difference in protonic stopping powers between aluminum and aluminum-oxide should not be contributing signifi-

cantly to the difference in the secondary-electron yields for the two materials. It follows that the secondary-electron mean free path in the materials is responsible for the difference in the yields. This is utilized to obtain a theoretical curve for the yield from aluminum-oxide as follows. Since the energy spectra of secondary electrons produced by primary electrons is similar to the energy spectra produced by primary ions (for example, see fig. 16 of ref. [18] and fig. 2 of ref. [19]), the mean free path of a typical electron-produced secondary electron in a material should be similar to the mean free path of a typical ion-produced secondary electron in that same material. This should be particularly true if the primary electron has the same velocity as the primary ion, the kinetics of the Coulomb collisions of the primaries with the electrons of the material then being very similar in the two cases. Bruining and de Boer [20] measured the secondary-electron yield for primary electrons with $E \leq$ 600 eV hitting clean aluminum targets and oxidized-aluminum targets. These primary electrons had velocities equal to the velocities of protons with $E \leq 1.1$ MeV, close to the energies of the present experiment. The ≤ 600 eV primary electrons in the Bruining and de Boer experiments had ranges in aluminum of ≤ 200 Å (see ref. [21]); these are long compared with the expected mean free paths of the secondaries in the material (see below), so slowing down of the primary electrons near the material's surface should not have affected the yield of secondaries. Bruining and de Boer found the secondary-electron yield from aluminum-oxide to be a factor of ~ 2.25 times larger than the yield from pure aluminum. To obtain an empirical curve for the yield of secondaries from aluminum-oxide $Y_{Al_2O_3}$, the theoretical yield from pure aluminum Y_{Al} is multiplied by 2.25, which gives

$$Y_{Al_2O_3} = 3.6 \times 10^{-9}\left(\frac{dE/dx}{\text{eV/cm}}\right)\left[1 + \frac{1}{1 + \dfrac{E}{0.183\ \text{MeV}}}\right]. \tag{6}$$

This corresponds to the mean free path of secondary electron in Al_2O_3 being $2.25/0.95 = 2.37$ times the mean free path in pure Al, which gives $L_s = 38.8$ Å. Thus, secondary electrons are able to escape from deeper within the aluminum-oxide than they are able to from aluminum. The empirical relation (6) is plotted in fig. 2; as can be seen, the measured data points of both the present experiment and of the earlier experiment of Mironov and Nemenov [13] fall near the curve. The different between the fit to the present data [eq. (2)] and the empirical curve [eq. (6)] is always $< 20\%$.

The agreement of the $H^+ \rightarrow$ Au data of the present experiment with the theory of Sternglass [15] is quite good (see fig. 3). Over the range of proton energies of the experiment, the fit to the data [eq. (3)] always agrees to within 5% with the theoretical curve [eq. (5)]. Note that whereas the Aarset et al. [14] data points agree fairly well with the theoretical curve for aluminum, they do not agree well with the curve for gold (see fig. 3). Neither do they continue the trend of the gold data of this experiment. For fast protons incident on various metal targets, Aarset et al. find little variation ($\sim 4\%$) in the secondary-electron yield over a variety of target types, including aluminum and gold. This is in contrast to other experiments, where substantial variations in the secondary-electron yields with target materials are found for high-velocity protons on metals (ref. [22]), intermediate-velocity ions on metals (ref. [23]), and high-velocity electrons on metals (ref. [24] and [25]). More data for fast protons on a variety of metal targets is desirable to settle this matter.

4. Discussion: effect of surface roughness

The surfaces of the targets are not perfectly smooth, hence the surfaces are composed of local regions that are tilted away from the surface normal. These tilts are expected to increase the secondary-electron yields over the values obtained from the normal-incidence theory as follows. For a surface whose normal is oriented at an angle θ with respect to the direction of incidence of the primaries, the portion of a primary's path that lies within L_s of the surface has a length of $L_s/\cos\theta$. Thus, the amount of energy deposited within L_s of the surface is $(dE/dx)L_s/\cos\theta$. Accordingly, in the secondary-electron-emission model of Sternglass [15] the yield of secondaries emitted when the surface has a tilt of θ compared with the yield at normal incidence is $Y(\theta)/Y(0°) = 1/\cos\theta$. A rough surface oriented normal to the beam can be modeled by a large number of small, randomly oriented surfaces. Taking the distribution of surface area with orientation angle to be uniform from $0°$ to θ_{max} and averaging the secondary-electron yield over random orientations of surfaces from $0°$ to θ_{max}, the yield is $\langle Y\rangle = (1/\theta_{max})\int_0^{\theta_{max}} Y(\theta)\,d\theta$, which gives

$$\langle Y\rangle = Y(0°)\frac{1}{\theta_{max}}\log\left[\tan\left(\frac{\pi}{4} + \frac{\theta_{max}}{2}\right)\right]. \tag{7}$$

This expected increase in the secondary-electron yield from rough surfaces may account for some of the difference between the data and the theory (see figs. 2 and 3). The fit to the aluminum data [eq. (2)] is $\sim 16\%$ higher than the theoretical prediction for the yield of secondaries from aluminum-oxide [eq. (6)], and the fit to the gold data [eq. (3)] is $\sim 5\%$ higher than the theoretical prediction for the yield of secondaries from gold [eq. (5)]. According to the above model, an increase in the emission by 16% over eq. (6) corresponds to $\theta_{max} \simeq 60°$ for aluminum and an increase in the emission by 5% over eq. (5) corresponds to $\theta_{max} \simeq 30°$ for gold.

The surface of the aluminum target was examined to ~ 1000 Å resolution via a scanning electron microscope that imaged secondary electrons generated by electron bombardment. Grooves of ~ 50000 Å width cover ~ 10% of the surface area and ~ 1% of the surface is covered by 10^4 Å-diameter pits. Also observed were a few ~ 10^5 Å-diameter outcrops that are very strong secondary-electron emitters under bombardment by the microscope's 5–19 keV electron gun; these may be similar to the crystalline outcrops known to form on hot aluminum in air [26]. The microscope showed the surface's secondary-electron emission to be patchy on the smallest spatial scales seen (~ 1000 Å), but also showed patchiness with 10^5–10^6 Å scale-sizes. It is not known whether this patchiness in the secondary-electron emission is owed to tilts in the surface or to changes in the composition or condition of the oxide layer. Other investigators examining the transmission of 100-keV electrons through the oxide layers on aluminum have observed irregularities down to 1000-Å spatial scales [27]; these small-scale irregularities were believed to be crystal sizes in the oxide. Since Al_2O_3 can form crystals (e.g. corundum or boehmite), there is a possibility that the small-scale topology of the surface is spiky. It is very desirable to know the topology of the surface on 50-Å scale sizes, however, for such metallic samples the resolution required to see this is not easily obtained with a scanning electron microscope. Earlier investigators [28] found the Al_2O_3 surface to be composed of two layers: a thin, nonporous, inner layer that may be either crystalline or amorphous and a thick, porous, outer layer that is most often amorphous. Because this outer layer is 50–1000 Å thick [8–10] and probably amorphous the surface roughness on 50-Å spatial scales is probably not determined by the crystalline nature of the Al_2O_3, but rather by the unknown roughness of the surface of the aluminum target material when it was extruded. It may, in fact, be the case that oxidation has smoothed the surface of the target [29].

The surface of the gold target was not examined with the scanning electron microscope. It is possible that its surface contains cubic crystals of gold, but a large fraction of the surface being covered with such crystals is inconsistent with the secondary-electron-yield data. For randomly oriented cubic crystals, the yield calculated from the $Y(\theta) \propto 1/\cos\theta$ relation is found to be $\langle Y \rangle = 1.273 Y(0°)$, which represents a 27.3% increase over the eq. (5) prediction. This increase is much larger than the ~ 5% discrepancy between eq. (5) and the data.

The authors wish to acknowledge Bob Baldonado, Mike Barron, Ted Fritz, Lloyd Hunt, Roger Life, Gary Luedemann, and Larry Rowton for their assistance. This work was supported by the US Department of Energy.

References

[1] H. Bruining, Physica 3 (1936) 1046.
[2] K.H. Krebs, Fortschritte der Physik 16 (1968) 419.
[3] A.W. Hull, Phys. Rev. 18 (1921) 31.
[4] H.H. Andersen and H.L. Bay, in: Sputtering by Particle Bombardment I, Physical Sputtering of Single-Element Solids, ed. R. Behrisch (Springer, Berlin, 1981) p. 143.
[5] H.L.Bay, J. Roth and J. Bohdansky, J. Appl. Phys. 48 (1977) 4722.
[6] B.V. Panin, Sov. Phys. JETP 15 (1962) 215.
[7] U. Littmark and J.F. Ziegler, Handbook of Range Distributions for Energetic Ions and All Elements, (Pergamon, New York, 1980).
[8] P.E. Blackburn and E.A. Gulbransen, J. Electrochem. Soc. 107 (1960) 944.
[9] D.G. Altenpohl, Corrosion 18 (1962) 143.
[10] H.P. Godard, W.P. Jepson, M.R. Bothwell, and R.L. Kane, The Corrosion of Light Metals (Wiley, New York, 1967) Table 1.1.
[11] C.N. Cochran and W.C. Sleppy, J. Electrochem. Soc. 108 (1961) 322.
[12] L.S. Frost and A.V. Phelps, Phys. Rev. 127 (1962) 1621.
[13] E.S. Mironov and L.M. Nemenov, Sov. Phys. JETP 5 (1957) 188.
[14] B. Aarset, R.W. Cloud, and J.G. Trump, J. Appl. Phys. 25 (1954) 1365.
[15] E.J. Sternglass, Phys. Rev. 108 (1957) 1.
[16] L.C. Northcliffe and R.F. Schilling, Nucl. Data Tables A7 (1970) 233.
[17] P. Marmier and E. Sheldon, Physics of Nuclei and Particles, vol I (Academic Press, New York, 1969), Section 4.10.
[18] R. Kollath, Ann. Phys. 39 (1941) 59.
[19] A.B. Laponsky, J. Appl. Phys. 34 (1963) 1568.
[20] H. Bruining and J.H. de Boer, Physica 5 (1938) 17.
[21] H.-J. Fitting, Phys. Status Solidi A26 (1974) 525.
[22] A.G. Hill, W.W. Buechner, J.S. Clark, and J.B. Fisk, Phys. Rev. 55 (1939) 463.
[23] L.N. Large and W.S. Whitlock, Proc. Phys. Soc. 79 (1962) 148.
[24] H. Bruining, Physics and Applications of Secondary Electron Emission, (McGraw-Hill, New York, 1954).
[25] B.F.J. Schonland, Proc. R. Soc. Lond. A104 (1923) 235.
[26] R.K. Hart and W.E. Ruther, J. Nucl. Mater. 4 (1961) 272.
[27] K. Thomas and M.W. Roberts, J. Appl. Phys. 32 (1961) 70.
[28] M.S. Hunter and P. Fowle, J. Electrochem. Soc. 103 (1956) 482.
[29] R.C. Plumb, J. Electrochem. Soc. 105 (1958) 502.